



OPEN

SUBJECT AREAS:

TRANSMISSION  
ELECTRON MICROSCOPY

COMPOSITES

Received  
10 September 2014Accepted  
20 November 2014Published  
9 December 2014Correspondence and  
requests for materials  
should be addressed to  
L.S. (lils2@cam.ac.uk)

# Electron tomography provides a direct link between the Payne effect and the inter-particle spacing of rubber composites

Lech Staniewicz<sup>1</sup>, Thomas Vaudey<sup>2</sup>, Christophe Degrandcourt<sup>2</sup>, Marc Couty<sup>2</sup>, Fabien Gaboriaud<sup>2</sup> & Paul Midgley<sup>1</sup><sup>1</sup>Department of Materials Science and Metallurgy, University of Cambridge, 27 Charles Babbage Road, Cambridge, CB3 0FS, United Kingdom, <sup>2</sup>Manufacture Française des Pneumatiques Michelin, 23 Place des Carmes Déchaux, 63040 Clermont Ferrand Cedex 9, France.

Rubber-filler composites are a key component in the manufacture of tyres. The filler provides mechanical reinforcement and additional wear resistance to the rubber, but it in turn introduces non-linear mechanical behaviour to the material which most likely arises from interactions between the filler particles, mediated by the rubber matrix. While various studies have been made on the bulk mechanical properties and of the filler network structure (both imaging and by simulations), there presently does not exist any work directly linking filler particle spacing and mechanical properties. Here we show that using STEM tomography, aided by a machine learning image analysis procedure, to measure silica particle spacings provides a direct link between the inter-particle spacing and the reduction in shear modulus as a function of strain (the Payne effect), measured using dynamic mechanical analysis. Simulations of filler network formation using attractive, repulsive and non-interacting potentials were processed using the same method and compared with the experimental data, with the net result being that an attractive inter-particle potential is the most accurate way of modelling styrene-butadiene rubber-silica composite formation.

Rubber tyres, whose use on wheeled vehicles is ubiquitous, are typically a complex construction using several components including reinforcing metal and/or textile wires and the rubber itself, which is a composite based on a polymer matrix plus various additives. Perhaps the most important rubber additives are hard filler particles, either carbon black or silica, which are responsible for improving the wear resistance<sup>1</sup> and stiffening the rubber<sup>2</sup>, leading to a longer service life and less energy loss from deformation (which is responsible for the rolling resistance of tyres and thus an increased fuel consumption).

The ability of filler particles to provide mechanical reinforcement was recognised in 1905 by using zinc oxide, but was quickly superseded as an “active” filler by carbon black in 1912 and silica in 1939<sup>1</sup>. There are advantages to using silica: for example, the wet skid resistance of silica-filled rubber can be higher than that of carbon black-filled rubber<sup>3</sup> and, as carbon black is generally produced from fossil fuels, silica may be regarded as a more environmentally sustainable alternative.

With fillers being a critical component of tyre manufacture, it is important to understand their function and the detailed role they play in tyre performance. Simple explanations for how filler particles function can be made using fluid dynamical arguments<sup>4</sup>, where a suspension of non-interacting incompressible monodisperse spheres in a liquid will exhibit a greater viscosity than the pure liquid on its own. Although the modified Guth and Gold equations<sup>4</sup> provide an improved description of the behaviour of fillers compared to the original Einstein equation<sup>5</sup>, one of the core assumptions (that the continuous phase is a fluid) is not valid for a crosslinked rubber matrix and so a more accurate description of rubber composite behaviour is required.

Filler particles, when properly incorporated into the matrix, will bond to this crosslinked network and locally immobilise the rubber, increasing the tensile strength. The stronger the rubber-filler interaction, the more pronounced this effect will be ref. 6. However, a balance must be struck, since covalent bonding between the crosslinked rubber matrix and the filler particles can be detrimental in the case of large strain values<sup>7</sup>; it is better



for the polymer chains to slide along the surface of the filler particles or desorb rather than undergo chain scission and damage the polymer network.

The existence of a volume fraction threshold of the filler for transitions in both mechanical<sup>8</sup> and electrical<sup>9</sup> (for conducting fillers, like carbon black) behaviour of the composite indicates that there is a critical particle density and hence an inter-particle spacing at which point the filler forms a percolating network. Filler particles do not need to physically touch in order for this transition to occur - a layer of “bound rubber” on the exterior of the particles has been postulated to increase the filler’s effective radius for the purpose of forming percolating networks through the material<sup>10–12</sup>. One key property of rubber-filler composites is that their shear modulus decreases as a function of strain<sup>2</sup> - this phenomenon is known as the Payne effect<sup>13</sup>.

Since the magnitude of the reinforcing and Payne effects is related to the proportion of particles which are close enough for their shells of bound rubber to interact, the distribution of inter-particle spacings should be an accurate descriptor of the filler’s reinforcement ability. The mechanical properties of rubber composites with varying bulk volume fractions of filler are regularly studied using rheology methods, but there has been little work to date on correlating macroscale physical properties with quantitative information from the nanoscale filler structure.

To that end, we have undertaken electron tomography<sup>14</sup> on rubber composite materials with a range of filler volume fractions, using pillar-shaped samples<sup>15,16</sup> produced using a focussed ion beam instrument (FIB) to minimise resolution loss due to occlusion at high tilt angles. In contrast to most previous electron microscopy of this material type<sup>17</sup>, we use high-angle annular dark-field scanning transmission electron microscopy (HAADF-STEM) to provide images with high-contrast<sup>18</sup>, improved resolution for relatively thick samples<sup>19</sup> and, where possible, diffraction contrast (from crystalline silica particles) is minimised<sup>14</sup>. For much thicker samples and/or those with species of higher atomic number, bright-field (BF) or annular bright-field (ABF) imaging may yield high quality images<sup>20</sup>. However, for beam-sensitive samples, where electron dose is important, detector sensitivity and noise is also a key factor and in our case the dark-field detector was significantly superior.

Pillars were produced with diameters ranging from 100–250 nm. Whilst larger pillars would be advantageous in terms of providing better statistics, the reconstruction quality will inevitably decrease as the sample size increases. Problems with large samples arise not only from image quality in the form of depth of field (the distance along the beam axis from the focal plane for which the sample will be “in focus”), but also from the fact that the overall 3D reconstruction resolution scales with sample size. The resolution can be estimated using the Crowther criterion<sup>21</sup>  $d = \frac{\pi D}{N}$ , where  $D$  is the diameter of the reconstruction volume and  $N$  is the number of projections taken. In practice, achievable resolution is better than the Crowther criterion would suggest<sup>22</sup>: 0.5–1 nm separations between particles can be seen in the reconstructions presented here, which is significantly better than the estimate of ca. 6 nm (150 nm diameter, 77 projections).

## Results and Discussion

**Reconstruction.** Figure 1a) is an example of the reconstructions obtained and shows the silica component of one pillar along with an example in Fig. 1b) of an individual aggregate, rendered using the UCSF Chimera software<sup>23</sup>. While the filler particles in this example appear very polydisperse and unevenly spaced, this may be an artefact of the pillar shape and the relatively small volume available for imaging within any individual pillar. The relatively large size of the silica aggregates compared to the pillar volume will lead to possible measurement errors. Because of this, we will only examine particle spacings, make no attempt to measure particle sizes and will

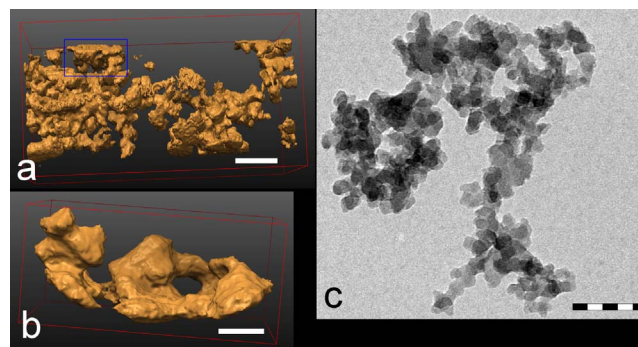


**Figure 1** | (a) a surface render of the silica in one reconstructed pillar. This portion of the pillar contains 16.2% silica by volume, is 369 nm long and has a diameter increasing smoothly from 165 to 185 nm. Scale bar: 100 nm. (b) A magnified view of a single “aggregate”, highlighted in blue in (a). Scale bar: 20 nm. (c) a single silica aggregate before mixing imaged using bright-field TEM. Scale bar: 100 nm.

only conduct direct comparisons between volumes of similar shape and size. A volume render of the same pillar prior to classification is shown in Supplementary Information.

In order to ensure the accuracy and objectivity of the silica volume measurement, we do not rely on a simple thresholding approach but instead classify the reconstruction into 3-level volumes using the Trainable Weka Segmentation<sup>24</sup> software (part of the freely available Fiji distribution of ImageJ<sup>25</sup>) - see Supplementary Information for further details. This machine learning approach allows us to identify parts of the volume based on local information and hence should provide a more accurate classification of the volume. A more complete explanation of the procedure, along with the difference between machine-learning methods and a 3-level Otsu thresholding operation<sup>26</sup> is shown in Supplementary Information. An animation showing each slice of the reconstructed and the classified pillar is also shown in Supplementary Video 1.

While compressed sensing (CS) and discrete tomographic reconstruction techniques can produce reconstructions which are already classified (a finite, discrete number of grey levels) and which are relatively insensitive to missing wedge artefacts or noise in the images<sup>27–29</sup>, they are still under considerable development and as such CS algorithms are not implemented in readily available software. Since the objective of this work was in part to develop methods to acquire and routinely process relatively large amounts of data, we decided to use readily available and mature software rather than more developmental code.

**Microscopy data.** Once classified, the volume can be segmented and processed to obtain quantitative information. We measure a “cumulative percolation” parameter defined as a function of particle spacing (explained in more detail in Supplementary Information) which factors in both the progress towards forming a continuous network and the proximity of individual particles. Examples of such percolation curves are shown in Fig. 2a). A perfect close packing “crystal” of monodisperse spherical particles would result in a step function for a cumulative percolation; inhomogeneous particle distribution (clustering), polydisperse particle sizes and non-spherical particle shapes act to smooth the transition. It should be noted that if the particles have a fractal nature<sup>30</sup>, spurious results may occur when a particle is not fully enclosed within the reconstructed volume - the portion which reaches inside may be two (or more) components of a “fork” and present an inter-“particle” separation unrelated to the actual particle spacing.

The curves shown in Fig. 2a) are all of a similar form. Ab initio, there is no analytical function that describes the curves but previous

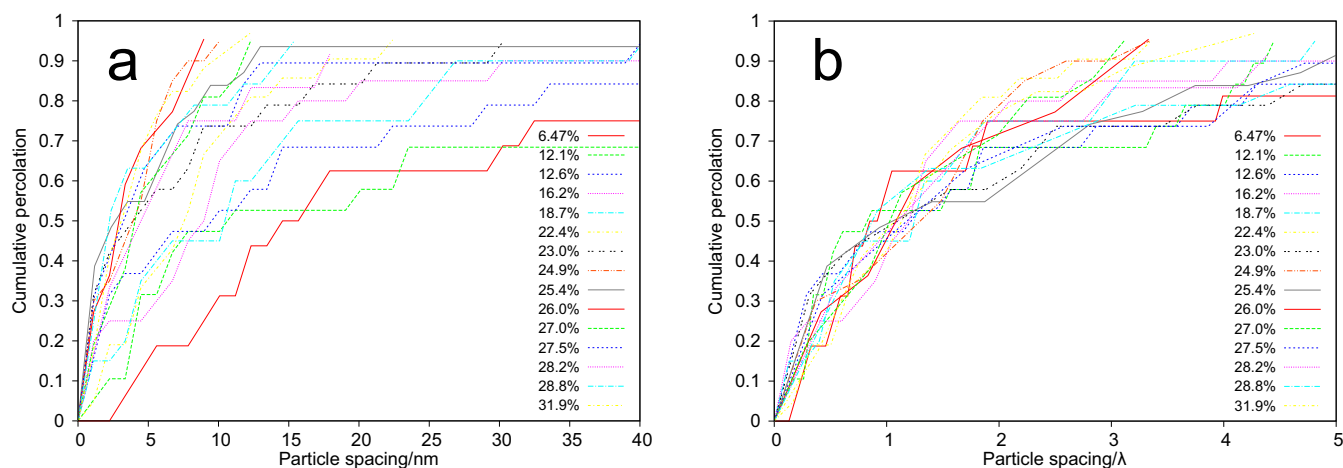


**Figure 2** | (a) Cumulative percolation curves for all samples (legend indicates the volume fraction of silica measured in each individual pillar) and (b) the same curves, scaled horizontally such that the median of fitted cumulative log-normal distributions coincide.

work on similar materials<sup>31,32</sup> has used a log-normal distribution to describe inter-particle spacings - applying this to our data, we find that the cumulative form of this distribution fits our percolation curves well. Because the individual percolation curves are noisy, extracting information from them directly will introduce error. To work around this, we fit a cumulative log-normal distribution to each percolation curve and then define a characteristic spacing,  $\lambda$ , as the median value of the fitted cumulative log-normal distribution (ie. where the cumulative distribution is equal to 0.5) - since fitting a curve uses the entire data set as opposed to interpolating from a few points around the middle, this should provide for a more accurate description of the median inter-particle spacing. In Fig. 2b), the curves in Fig. 2a) have been normalised by the characteristic spacing  $\lambda$ . The similarity between the curves in Fig. 2b) provides confidence in the ensemble of data, even though individual measurements may have error, and evidence that a simple scaling relationship may exist between the volume fraction and particle spacing. At high values of particle spacing, there is a greater spread across the curves, with low volume fraction data giving rise to relatively low values of the cumulative percolation, and high volume fraction data, higher values.

**Simulation data.** The variation in the characteristic spacing,  $\lambda$ , can then be examined as a function of filler volume fraction, as shown in Fig. 3. Each experimental point corresponds to a single reconstructed pillar sample and the volume fraction to the measured value in the reconstructed volume. To interpret this curve, we have fitted the data to a simple function derived by Ambrosetti et al through the distribution of non-interacting prolate spheroids<sup>33</sup>. Ambrosetti and co-workers showed that to a good approximation a critical cutoff distance,  $\delta$ , analogous to our characteristic spacing,  $\lambda$  can be related to the volume fraction  $\phi$  by

$$\delta = \frac{0.8a \left(\frac{b}{a}\right)^2}{\phi(1+8\phi)} = \frac{A}{\phi(1+8\phi)} \quad (1)$$

where  $a$  and  $b$  are the major and minor radii of the prolate spheroid. A best-fit curve to the data, shown in Fig. 3, was found with  $A = 2.75 \pm 0.19$  (error is the asymptotic standard error in a non-linear least squares fit). The raw data (volume fraction,  $\mu$ ,  $\sigma$ , fitting errors, where  $e^\mu = \lambda$ ) for each pillar is shown in Supplementary Table 1.

Further to this, we simulated the formation of rubber-silica composites at silica volume fractions of 14%, 16%, 18%, 20% and 22% with 10 simulations made for each volume fraction. Simulations were conducted in a cubic cell under three conditions - non-interacting, repulsive and attractive particles. To provide a direct comparison

with experimental data, cylindrical volumes (150 nm in diameter) were extracted from the cubic cell and processed in the same way as the experimental data, obtaining cumulative percolation curves (examples from each simulation type are shown in Supplementary Information) and characteristic spacings, which are plotted as a function of measured volume fraction alongside the experimental data in Fig. 3.

All three simulations can be fitted with curves of the same form as equation 1. The best fit to non-interacting particles is found with  $A = 1.49 \pm 0.04$ , repulsive particles with  $A = 5.69 \pm 0.07$  and attractive particles with  $A = 2.74 \pm 0.08$ . As with the experimental data, errors are the asymptotic standard error from a non-linear least squares fit. Because the particles do not deform during simulation, the major and minor radii  $a$  and  $b$  in the original definition of  $A = 0.8 \frac{b^2}{a}$  should be seen as effective sizes which also contain information about inter-aggregate interactions. Additionally, the constrained anisotropic nature of the sample volume means that any lengths extracted will not necessarily be representative of a “real” sample. However, the fitting constant  $A$  is still useful when comparing the three simulation types with experimental data. The attractive inter-aggregate potential provides an extremely close match to the experimental data - both visually, when overlaying the data points and numerically, when comparing the fitting constants. The choice of potentials was purely empirical - prior to conducting these experiments, we had no evidence for or against the different types of inter-particle potential. So far, we see that the attractive potential is the best match for our system, but further work is required to determine whether an attractive inter-particle potential is universally applicable for all rubber-filler composite systems or only for the specific silica-SBR composite investigated here.

It should be noted that the range of calculated volume fractions from the experimental data (6%–32%) is smaller than the range of simulated volume fractions. This is due to a difference in the initial conditions of the experimental and the simulated data. For the simulations, the material starts as a completely random distribution of particles which is then allowed to evolve under a given potential. Manufacturing the rubber composite, on the other hand, is done by adding silica powder to rubber (the initial state is therefore completely phase-separated) and then mixing repeatedly. The high viscosity of rubber makes it impractical to obtain a completely even distribution of silica particles purely by mixing - either the mixing time would be extremely long, or the polymer matrix would be damaged by a more vigorous mixing. Additionally, the viscosity of the rubber acts to screen any effective potential between the particles, meaning that any silica further than approximately 50 nm apart essentially will not interact and therefore nanoscale inhomogeneities

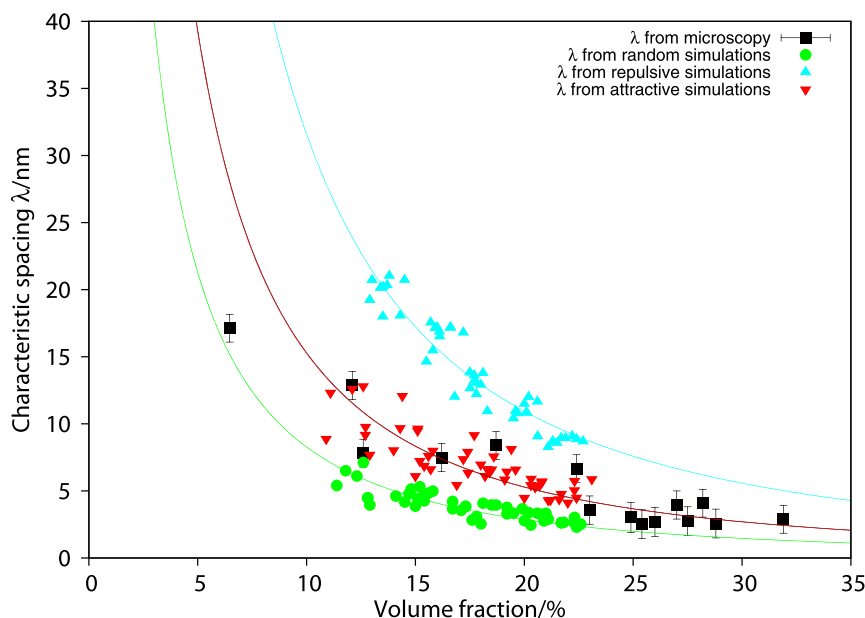


**Figure 3** | A comparison between experimental results (large squares) and rubber composite simulated under attractive, repulsive and random filler distribution conditions. Continuous lines are fits to an equation of the form  $y = \frac{A}{\phi(1+8\phi)}$ , where  $\phi$  is the volume fraction and  $A$  is a free parameter. Error bars on the microscopy data are fitting errors when applying the cumulative log-normal distribution to each percolation curve.

on the scale of our pillar samples will remain. The range of simulated volume fractions could have been increased, but the resulting initial conditions will not be representative of the bulk or mesoscale sample (on this scale, the silica volume fraction matches the bulk volume fraction) and as such we chose to limit our simulation range to bulk volume fractions representative of the manufactured rubber composite.

**Mechanical data.** Having obtained a relationship between volume fraction and median inter-particle spacing, we can combine this data with a conventional mechanical analysis to obtain a direct link between the mechanical properties of a rubber composite and the inter-particle spacing. Fig. 4 shows the magnitude of the shear modulus,  $G^*$ , plotted as a function of shear strain for different volume fractions of the elastomer/silica system used in this work. The trend of increasing shear modulus with filler volume fraction, along with decreasing shear modulus with strain magnitude is standard behaviour for this class of material.

Figure 5 shows how the magnitude of the Payne effect in our three samples, defined here as  $\Delta G_{norm}^* = \frac{G_{max}^* - G_{min}^*}{G_{min}^*}$ , where  $G_{max}^*$  is the maximum value of  $G^*$  (located at minimum strain) and  $G_{min}^*$  is the minimum value of  $G^*$  (located at maximum strain), varies with respect to both the bulk volume fraction (Fig. 5a) and the median inter-particle spacing (Fig. 5b) as determined from Equation 1 with  $A = 2.75$ . Previous work<sup>34</sup> has observed a power law relationship between mechanical reinforcement (proportional to the Payne effect, which is a reduction in reinforcement behaviour) and volume fraction, so we assume a similar form and find that  $\Delta G_{norm}^* \propto \phi^{2.3 \pm 1.1}$ , or  $\Delta G_{norm}^* \propto \lambda^{-1.5 \pm 0.6}$ , which are comparable to the values obtained by Baeza et al<sup>34</sup>.

It should be noted that although power law relationships can be obtained between the absolute value of  $G^*$  at one strain value and  $\phi$  or  $\lambda$ , the exponent will vary depending on which strain value is taken. If we take the 0.1% strain point, we obtain  $G^* \propto \phi^{3.4 \pm 0.7}$ , a similar value to the zero shear rate relationship of  $G \propto \phi^{3.5}$  predicted by Cassagnau on silica-filled polymer melts<sup>35</sup>. In this work, we have used electron tomography with an alternative image analysis technique to

provide a direct link between inter-particle spacing in a rubber-filler composite and the mechanical properties of said composite. We have also used these spacing measurements to show that an attractive inter-particle force is the most accurate model when simulating the formation of this type (Silica-SBR) of rubber-filler composite. These results enable rubber manufacturers to design new materials with an improved prior estimation of the material's properties, potentially leading to faster development cycles or a more accurately tailored material.

## Methods

**Materials.** Silica-SBR nanocomposites are formulated by stepwise introduction and mixing of SBR ( $M_w = 140 \text{ kg mol}^{-1}$ ,  $PI = 1.07$ , density =  $0.94 \text{ g cm}^{-3}$ , statistical copolymer with 26% wt styrene and 74% wt butadiene units (41% of which are 1–2 and 59% are 1–4) chains with silica pellets (Zeosil 1165 MP from Solvay) in an internal mixer (ThermoHaake). Particular care was taken to avoid any trace of carbon black or ZnO nanoparticles. The mixing chamber is preheated and the rotor speed is adjusted during the process to between 95 and 105 RPM as a function of nanocomposite composition in order to obtain the same final mixing temperature of  $165 \pm 5^\circ\text{C}$ . The polymer is introduced first, in the form of centimetric lamellae. After about 1 min, the mixture of silica pellets, DiPhenylGuanidine (Vulcavit from Bayer, 1.5% wt with respect to polymer), the liquid mixture of coupling and coating agent (OCTEO from Dynasylan, 8% wt with respect to silica, bis-TriEthoxySilylPropylTetrasulfide from Evonik, 4% wt with respect to silica) and oil (30% wt with respect to polymer) are incorporated via the same piston. The process is finished after typically 5 min. The hot sample is then rapidly cooled by lamination 4 times and homogenized 12 times after introduction of a crosslinking agent (DiCumylPeroxide 2% wt with respect to polymer) in the 1 mm gap of a two roll mill. The materials are molded in 1 mm thick sheets and cured at  $160^\circ\text{C}$  for 20 minutes to obtain the final crosslinked materials. 3 materials were produced with target silica volume fractions of 15%, 20% and 25%. The silica volume fractions in the nanocomposites were confirmed by thermogravimetric analysis (Mettler Toledo) using a first ramp at  $50 \text{ K min}^{-1}$  from 25 to  $550^\circ\text{C}$  under nitrogen, followed by a second ramp at  $10 \text{ K min}^{-1}$  from 550 to  $750^\circ\text{C}$  under air. Using a density of silica of  $2.06 \text{ g cm}^{-3}$ , the macroscopic volume fraction obtained for the 15%, 20% and 25% samples is respectively equal to 13.8%, 18.6% and 23.8%

**Pillar preparation.**  $3 \times 3 \times 1 \text{ mm}$  sections of rubber composite material were cut with a scalpel and attached to an SEM stub using conductive carbon cement with the cut  $3 \times 3 \text{ mm}$  side facing upwards. After allowing the carbon cement to dry in atmosphere for 1 day, the samples were then coated with gold using an Emitech K550 sputter coater for 5 minutes at 20 mA.  $15 \times 10 \times 2 \mu\text{m}$  lamellae were milled from the samples using an FEI Helios Nanolab dual-beam FIB-SEM instrument using the supplied AutoTEM software. Each lamella was cut out and platinum-welded to the tip of the central finger on an Omniprobe TEM grid, then thinned into a single  $2 \mu\text{m}$  long  $\times$  100 nm diameter cylindrical pillar pointing along the axis of the Omniprobe grid finger.

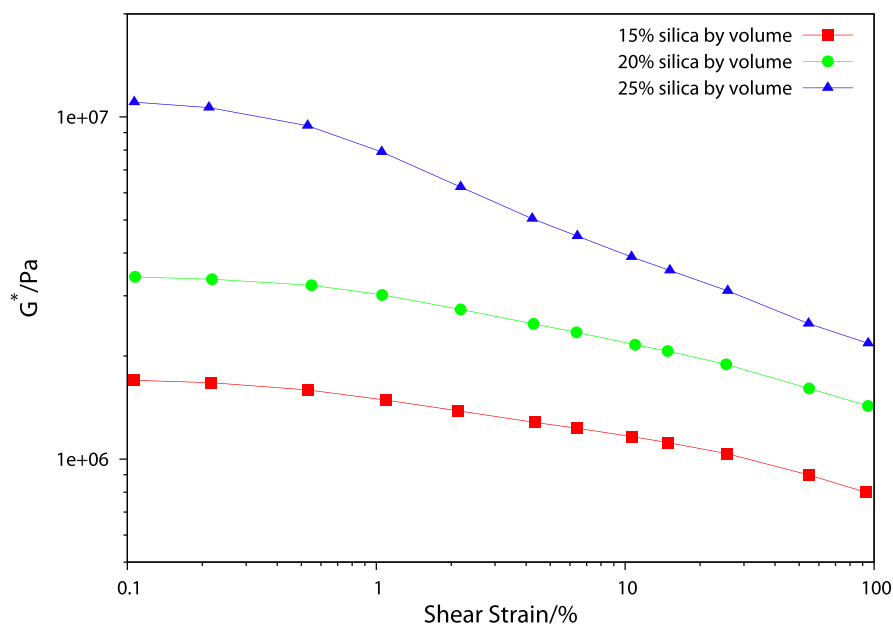


**Figure 4** | Shear modulus  $G^*$  versus shear strain curves for 15%, 20% and 25% volume fraction silica samples.

**Electron microscopy and 3D volume reconstruction.** Fabricated pillars on Omniprobe grids were loaded on to a Fischione 2020 high-tilt TEM holder and placed in an FEI Tecnai F20ST the day before imaging was to take place. The microscope was pumped down to operating vacuum and left overnight (15 h) to remove volatile components from the pillar. The pillar was tilted about its long axis and images taken from  $-76^\circ$  to  $+76^\circ$  of tilt at  $2^\circ$  increments using the FEI Explore3D software to form a complete tilt series. Images were taken in HAADF-STEM mode (detector acceptance angle:  $23.7\text{--}118$  mrad) with an accelerating voltage of 200 kV, a resolution of  $1024 \times 1024$  and a pixel size of 0.56 nm, imaging an area  $573 \times 573$  nm in size. Complete tilt series were aligned by a cross-correlation method and reconstructed into a 3D volume with 20 iterations of the SIRT algorithm<sup>36</sup>, using the FEI Inspect3D software for both procedures.

**Image processing.** Reconstructions were classified into 3-level volumes of vacuum, rubber and silica using the Trainable Weka Segmentation software, a component of the Fiji distribution of ImageJ. A subset consisting of every 15<sup>th</sup> slice along the pillar long axis was taken and Trainable Weka Segmentation trained on this subset using the Gaussian Blur, Difference of Gaussians, Sobel filter, Laplacian filter, Derivatives, Gabor filter, Structure Tensor, Membrane Projections, Hessian Matrix, Variance, Anisotropic Diffusion, Bilateral filter, Kuwahara filter, Entropy and Neighbours training features. The settings were left on their default values (membrane thickness: 1, membrane patch size: 19, minimum sigma: 1.0, maximum sigma: 16.0, classifier: fast random forest of 200 trees with 2 features per tree) Once training was complete, the classifier was applied to the complete image stack. 3-level volumes produced by Trainable Weka Segmentation were then processed using a custom-written C++

program, which segments the volume into separate objects according to adjacency in a  $3 \times 3$  cube centred on each voxel, each object corresponding to one filler “particle”.

Because the classification procedure is not perfect, it produces a large number of very small “objects” with sizes from one voxel upwards. Before any further processing is carried out, anything containing less than 300 voxels (corresponding to an equivalent spherical diameter of 4.6 nm) is removed from the volume - no particle was observed to be smaller than this in microscopy or simulations. The remaining objects are then dilated by 1 voxel each in the x, y and z directions and this process repeated until only one object remains. The final data is presented as  $1 - (\text{current object count} / \text{original object count})$  against the particle spacing (defined as  $2 \times \text{number of dilation steps} \times \text{voxel size}$ ) to track the progress towards forming a complete network of filler particles. All curve fitting was carried out using a non-linear least squares algorithm implemented in the gnuplot software.

**Simulations.** Zeosil 1165MP precipitated silica is composed of aggregates of primary particles, reinforced by an external layer of silica. The virtual reconstructed aggregates are modelled as aggregates of interpenetrated spherical particles. To generate representative 3D dispersion of silica, a library of aggregates was generated by using a Reverse Monte Carlo technique matching TEM microscopy images (Philips CM200, 200 kV, Bright Field,  $1 \text{ nm pixel}^{-1}$ ) of a large number of silica aggregates. The sample was prepared by adding 6 mg of powder to 40 mL of water followed by using a sonification probe (600 W for 10 minutes in a pulse mode 1 s/1 s) to break the silica pellets into single aggregates. Then a  $10 \mu\text{l}$  solution of this material was placed on a microscopy grid with formvar/carbon membrane made hydrophilic by a glow discharge before deposition. The radius of primary particles follows a log-normal

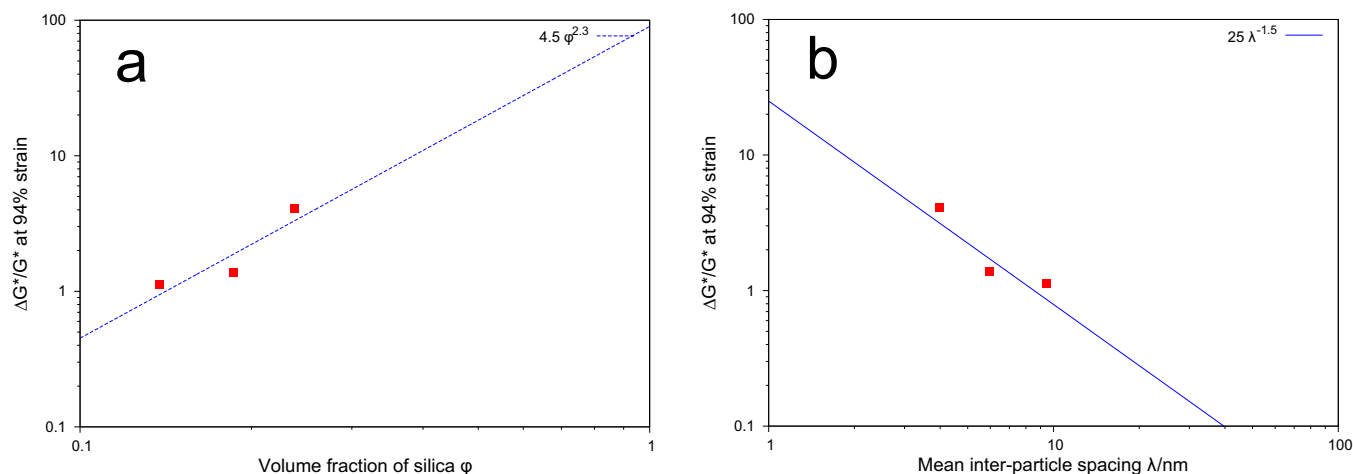


**Figure 5** | Scaling law relating the magnitude of the Payne effect with (a) the bulk filler volume fraction and (b) the median inter-particle spacing as measured by electron tomography.



distribution with  $\mu = 2.12$  and  $\sigma = 0.3$  (median = 8.3 nm, standard deviation = 2.7 nm). Arbitrary minimal and maximal radius cutoff values of 5 and 15 nm respectively are introduced to avoid unrealistic reconstruction of aggregates with either a large number of small particles or single particles with large diameters.

Around 8500 aggregates were reconstructed using a Diffusion Limited Aggregation algorithm matching the distribution of TEM aggregate projected surface with around 190000 primary particles. The mean aggregation number is thus equal to 22 and the maximum number of particles per aggregate has been set equal to 200.

A random dispersion of the 8500 aggregates was obtained at a desired volume fraction by sequentially selecting random aggregates in the library, randomly selecting a position of the center of mass in the cubic cell (size ranges from 1340 to 1560 nm, depending on the desired volume fraction) and an orientation with an acceptance criterion of non-overlapping particles with the former accepted aggregates. In the present case, the algorithm fails for a volume fraction of 24% with a threshold of  $10^6$  trials. The random dispersion of rigid aggregates is equilibrated using a Mesoscale Dynamics for non-Brownian suspensions in-house code at constant volume using a potential of mean force between the individual particles. Two limiting potentials were investigated, an attractive potential ( $U = e^{-\frac{h}{0.085}} - \frac{1}{30} e^{-\left(\frac{h}{0.85}\right)^2}$ , the first part represents hard-core repulsion and prevents interpenetration) that generates for the considered volume fraction a percolated network and a purely repulsive potential ( $U = e^{\frac{h}{0.85}}$ ) that maximizes the inter-aggregate distances, where  $U$  is the potential energy in Joules and  $h$  is the surface-surface distance in nm. Copies of the cubic volumes are also taken as-is to investigate the effect of a purely random aggregate distribution.

**Mechanical characterisation.** The crosslinked Silica-SBR nanocomposites were characterized using Dynamical Mechanical Analysis in a simple shear mode at 60°C and 10 Hz on a METRAVIB RDS VA4000 Visco Analyser. A first strain sweep from 0.1% to 100% peak-to-peak amplitude was imposed to the virgin sample and a second strain sweep from 100% to 0.1% peak-to-peak amplitude was sequentially recorded. The stress-strain raw data were analyzed using the standard METRAVIB DYNATEST procedure to extract the elastic ( $G'$ ) and loss ( $G''$ ) moduli of the materials. We define the Payne effect amplitude by the difference in shear modulus between the low and high strain amplitude  $G^*(0.1\%) - G^*(100\%)$  after an initial 100% strain accommodation thus from the second strain sweep. It is also associated with a maximum in the loss modulus and could be characterized by the amplitude at the maximum of the loss angle ( $\tan\delta = \frac{G''}{G'}$ ). The first strain sweep at increasing amplitude has not been used in the present analysis combining Payne effect and material damage known as the Mullins effect.

- Blow, C. M. & Hepburn, C. (eds.). *Rubber Technology and Manufacture* (Butterworth Scientific, London, 1982), 2nd ed.
- Payne, A. R. The dynamic properties of carbon black-loaded natural rubber vulcanizates. part I. *J. Appl. Polym. Sci.* **6**, 57. DOI:10.1002/app.1962.070061906 (1962).
- Wang, Y.-X., Ma, J.-H., Zhang, L.-Q. & Wu, Y.-P. Revisiting the correlations between wet skid resistance and viscoelasticity of rubber composites via comparing carbon black and silica fillers. *Polym. Test.* **30**, 557. DOI:10.1016/j.polymertesting.2011.04.009 (2011).
- Guth, E. & Gold, O. On the hydrodynamical theory of the viscosity of suspensions. *Phys. Rev.* **53**, 322 (1938).
- Einstein, A. Eine neue bestimmung der moleküldimensionen. *Ann. Phys. (Berlin)* **324**, 289. DOI:10.1002/andp.19063240204 (1906).
- Sadasivuni, K. K., Saiter, A., Gautier, N., Thomas, S. & Grohens, Y. Effect of molecular interactions on the performance of poly(isobutylene-co-isoprene)/graphene and clay nanocomposites. *Colloid Polym. Sci.* **291**, 1729. DOI:10.1007/s00396-013-2908-y (2013).
- Wang, Z., Liu, J., Wu, S., Wang, W. & Zhang, L. Novel percolation phenomena and mechanism of strengthening elastomers by nanofillers. *Phys. Chem. Chem. Phys.* **12**, 3014. DOI:10.1039/B919789C (2010).
- Yurekli, K. *et al.* Structure and dynamics of carbon black-filled elastomers. *J. Polym. Sci. Part B Polym. Phys.* **39**, 256 (2001).
- Miyasaka, K. *et al.* Electrical conductivity of carbon-polymer composites as a function of carbon content. *J. Mater. Sci.* **17**, 1610. DOI:10.1007/BF00540785 (1982).
- Ramorino, G., Bignotti, F., Pandini, S. & Riccò, T. Mechanical reinforcement in natural rubber/organoclay nanocomposites. *Compos. Sci. Technol.* **69**, 1206. DOI:10.1016/j.compscitech.2009.02.023 (2009).
- Jouault, N. *et al.* Well-dispersed fractal aggregates as filler in polymer-silica nanocomposites: Long-range effects in rheology. *Macromolecules* **42**, 2031. DOI:10.1021/ma801908u (2009).
- Leblanc, J. L. Rubber-filler interactions and rheological properties in filled compounds. *Prog. Polym. Sci.* **27**, 627. DOI:10.1016/S0079-6700(01)00040-5 (2002).
- Merabia, S., Sotta, P. & Long, D. R. A microscopic model for the reinforcement and the nonlinear behavior of filled elastomers and thermoplastic elastomers (payne and mullins effects). *Macromolecules* **41**, 8252. DOI:10.1021/ma8014728 (2008).

- Midgley, P. & Weyland, M. 3D electron microscopy in the physical sciences: the development of z-contrast and EFTEM tomography. *Ultramicroscopy* **96**, 413. DOI:10.1016/S0304-3991(03)00105-0 (2003).
- Kawase, N., Kato, M., Nishioka, H. & Jinnai, H. Transmission electron microtomography without the “missing wedge” for quantitative structural analysis. *Ultramicroscopy* **107**, 8. DOI:10.1016/j.ultramic.2006.04.007 (2007).
- Kato, M. *et al.* Maximum diameter of the rod-shaped specimen for transmission electron microtomography without the “missing wedge” *Ultramicroscopy* **108**, 221. DOI:10.1016/j.ultramic.2007.06.004 (2008).
- Kohjiya, S., Katoh, A., Suda, T., Shimanuki, J. & Ikeda, Y. Visualisation of carbon black networks in rubbery matrix by skeletonisation of 3d-tem image. *Polymer* **47**, 3298. DOI:10.1016/j.polymer.2006.03.008 (2006).
- Thomas, J. M. *et al.* The chemical application of high-resolution electron tomography: Bright field or dark field? *Angew. Chem. Int. Ed.* **43**, 6745. DOI:10.1002/anie.200461453 (2004).
- de Jonge, N. & Ross, F. M. Electron microscopy of specimens in liquid. *Nat. Nano.* **6**, 695 (2011).
- Motoki, S. *et al.* Dependence of beam broadening on detection angle in scanning transmission electron microtomography. *Journal of Electron Microscopy* **59**, S45. DOI:10.1093/jmicro/dfq030 (2010).
- Crowther, R. A., DeRosier, D. J. & Klug, A. The reconstruction of a three-dimensional structure from projections and its application to electron microscopy. *Proc. R. Soc. A* **317**, 319. DOI:10.1098/rspa.1970.0119 (1970).
- Loos, J. *et al.* Electron tomography on micrometer-thick specimens with nanometer resolution. *Nano Lett.* **9**, 1704. DOI:10.1021/nl900395g (2009).
- Pettersen, E. F. *et al.* UCSF Chimera - A visualization system for exploratory research and analysis. *J. Comput. Chem.* **25**, 1605. DOI:10.1002/jcc.20084 (2004).
- Hall, M. *et al.* The WEKA Data Mining Software: An Update. *SIGKDD Explorations* **11**, 10 (2009).
- Schindelin, J. *et al.* Fiji: an open-source platform for biological-image analysis. *Nat Meth* **9**, 676 (2012).
- Otsu, N. Threshold selection method from gray-level histograms. *IEEE Trans. Syst., Man, Cybern.* **9**, 62 (1979).
- Batenburg, K. *et al.* 3d imaging of nanomaterials by discrete tomography. *Ultramicroscopy* **109**, 730. DOI:10.1016/j.ultramic.2009.01.009 (2009).
- Goris, B., den Broek, W. V., Batenburg, K., Mezerji, H. H. & Bals, S. Electron tomography based on a total variation minimization reconstruction technique. *Ultramicroscopy* **113**, 120. DOI:10.1016/j.ultramic.2011.11.004 (2012).
- Leary, R., Saggi, Z., Midgley, P. A. & Holland, D. J. Compressed sensing electron tomography. *Ultramicroscopy* **131**, 70. DOI:10.1016/j.ultramic.2013.03.019 (2013).
- Schneider, G. J. *et al.* Influence of the matrix on the fractal properties of precipitated silica in composites. *J. Appl. Crystallogr.* **45**, 430. DOI:10.1107/S0021889812008631 (2012).
- Luo, Z. P. & Koo, J. H. Quantifying the dispersion of mixture microstructures. *J. Microsc.* **225**, 118. DOI:10.1111/j.1365-2818.2007.01722.x (2007).
- Luo, Z. & Koo, J. Quantification of the layer dispersion degree in polymer layered silicate nanocomposites by transmission electron microscopy. *Polymer* **49**, 1841. DOI:10.1016/j.polymer.2008.02.028 (2008).
- Ambrosetti, G. *et al.* Solution of the tunneling-percolation problem in the nanocomposite regime. *Phys. Rev. B* **81**, 155434. DOI:10.1103/PhysRevB.81.155434 (2010).
- Baeza, G. P. *et al.* Multiscale filler structure in simplified industrial nanocomposite silica/SBR systems studied by SAXS and TEM. *Macromolecules* **46**, 317. DOI:10.1021/ma302248p (2013).
- Cassagnau, P. Payne effect and shear elasticity of silica-filled polymers in concentrated solutions and in molten state. *Polymer* **44**, 2455. DOI:10.1016/S0032-3861(03)00094-6 (2003).
- Gilbert, P. Iterative methods for the three-dimensional reconstruction of an object from projections. *J. Theor. Biol.* **36**, 105. DOI:10.1016/0022-5193(72)90180-4 (1972).

## Acknowledgments

L.S. and P.A.M. thank Michelin for funding. The research leading to these results has received funding from the European Research Council under the European Union's Seventh Framework Programme (FP7/2007–2013)/ERC grant agreement 291522-3DIMAGE.

## Author contributions

L.S. performed sample preparation, microscopy and image processing. T.V. and C.D. assisted with the sample preparation. M.C. conducted the simulations. F.G. conducted the mechanical testing. L.S. and M.C. wrote the program code. L.S. analysed the data. M.C., F.G. and P.M. assisted with the analysis. L.S., M.C. and P.M. wrote the paper.

## Additional information

**Supplementary information** accompanies this paper at <http://www.nature.com/scientificreports>

**Competing financial interests:** T.V., C.D., M.C. and F.G. work for Michelin, who produce



the material analysed in this work. L.S. received funding from Michelin to carry out these experiments.

**How to cite this article:** Staniewicz, L. *et al.* Electron tomography provides a direct link between the Payne effect and the inter-particle spacing of rubber composites. *Sci. Rep.* **4**, 7389; DOI:10.1038/srep07389 (2014).



This work is licensed under a Creative Commons Attribution-NonCommercial-ShareAlike 4.0 International License. The images or other third party material in this article are included in the article's Creative Commons license, unless indicated otherwise in the credit line; if the material is not included under the Creative Commons license, users will need to obtain permission from the license holder in order to reproduce the material. To view a copy of this license, visit <http://creativecommons.org/licenses/by-nc-sa/4.0/>